LU-TP 21-06
January 2020

Quartic Higgs self-coupling at a 100 TeV pp collider

Sebastian Grabowski

Department of Astronomy and Theoretical Physics, Lund University

Master thesis supervised by Rikkert Frederix and Ioannis Tsinikos

Abstract

We present a parton-level phenomenological study of triple-Higgs production at leading order in proton-proton collisions at a center-of-mass energy of 100 TeV with an integrated luminosity of 30 ab^{-1}. This study aims to estimate the prospects for measuring the signal hhh production observable at the Future Circular Collider. We explore interesting final states that could be used for this purpose and focus our study on the $hhh \to \gamma\gamma b\bar{b}b\bar{b}$ final state. We construct a baseline analysis and investigate the signal sensitivity to simple deformations of the Higgs potential in the presence of the dominating non-resonant background. From this, we are able to demonstrate the sensitivity of the $pp \to hhh \to \gamma\gamma b\bar{b}b\bar{b}$ process to quartic Higgs coupling.

Popular Science Summary

The existence of the Higgs boson was confirmed in 2012, adding the last missing puzzle piece to the Standard Model of Particle Physics, our most accurate description of interactions between the fundamental building blocks of nature. However, even though the Higgs boson's mass has been measured, there are still open questions left to address. One of these questions is how the Higgs boson interacts with itself.

What we can learn about the Higgs self-interaction is directly linked to the so-called electroweak symmetry breaking mechanism, which allows the electroweak bosons ($W^{\pm}$ and Z^0 bosons) to become massive. For the mechanism to work, there must exist both three- and four-particle interaction couplings for the Higgs boson, yet to be measured. Their values have profound implications for Beyond the Standard Model physics and cosmology, particularly to the phase transition where the two, electromagnetic and weak, forces become separated in the early universe. So, a comparison of the measured and predicted Higgs boson self-interaction couplings provides the ultimate test of the Standard Model and its extensions.

This task is a difficult one, as we need to experimentally observe the production of several Higgs bosons in the same collision - a rare occurrence to say at least - and to make sure that they are produced from an intermediate Higgs boson, due to a self-interaction, rather than radiated from other particles. Experimentally, these two types of production are indistinguishable. Indeed there is no way of knowing what has occurred after the primary collision by detecting the shower of final-state particles in our detectors. Thus, one would need to measure the production precisely to compare it to theoretical predictions to understand how much of the signal comes due to the Higgs self-interactions. However, measuring the three-Higgs self-interaction at the LHC might not be possible, and previous studies have shown that the four-Higgs vertices are beyond our current grasp at the LHC as well.

There is still hope for determining the coupling strengths at the recently proposed post-LHC particle accelerator called the Future Circular Collider. At its collision energy of 100 TeV, it is believed that a precise measurement of Higgs self-interaction can be achieved. As for now, we need to develop a strategy for extracting this information about the couplings from the corresponding observables. There exist many difficulties along the way, and with this study, we will determine how feasible such an analysis would be.

Contents

1 Introduction

The existence of the Higgs boson was confirmed in 2012 by the ATLAS and CMS collaborations [1, 2]. Its mass was measured at 125 GeV [3], and its gauge and Yukawa couplings fall within the uncertainty Standard Model predictions within $10 - 15\%$ of the current experimental uncertainty [4]. The mass measurement of the Higgs boson was the first experimental step towards determining the structure of the Higgs potential. The next step is to determine the Higgs self-couplings.

From a theoretical point of view, determining the Higgs self-couplings is one of the most fundamental issues today [5, 6, 7]. In the framework of the Standard Model, the scalar self-couplings are completely determined by the mass of the Higgs boson and the Higgs vacuum expectation value. Thus, if there are substantial deviations from the Standard Model predictions for the Higgs self-couplings, this would mean that there is Beyond the Standard Model (BSM) physics. There are many predictions from BSM physics, some of which are discussed in Ref. [8]. For this reason, great efforts are made in investigating the self-coupling of the Higgs boson at present colliders in various scenarios BSM [9].

The prospects of precision measurement of the Higgs self-coupling are not entirely achievable with our current capabilities [10]. The reason is that the processes involving Higgs self-couplings are rare [11, 12]. These multiple-Higgs production processes are the double Higgs production relevant for accessing the cubic self-coupling [13] and the triple Higgs production necessary to study the quartic Higgs coupling. The reason for the low production rates is that there is a strong Higgs propagator suppression and the phase space is small due to the production of several heavy particles in the final state. There have been studies [14, 15, 16] investigating the potential of detecting the signal over the background in various Higgs decay channels for the Higgs pair production process at the high-luminosity phase [17] at the Large Hadron Collider (LHC). However, the triple Higgs production has a cross-section that is 2 orders of magnitude smaller with respect to the double-Higgs production, making the process more relevant to study at significantly higher collision energies. This task is left for the post-LHC era, for which different options are being discussed today. In this work, we explore the opportunities that are inherent to a new accelerator, the so-called Future Circular Collider (FCC) [18]. We investigate triple Higgs production in the gluon fusion channel in proton-proton collisions at a center-of-mass energy of 100 TeV and consider statistics of 30 ab^{-1} of data. The investigation is based on Monte Carlo simulations, where we generate and analyze both background and signal events.

This thesis is set up as follows. Section 2 contains the description of the theoretical framework that we have adopted in our study. The details of the Monte Carlo simulation and event generation are described in Section 3. Triple Higgs production modes and final states of interest are presented here. In Section 4.1, we present the event selection strategy and the differential distributions at parton level for triple Higgs boson production in the $\gamma\gamma b\bar{b}b\bar{b}$ channel at 100 TeV are shown in Section 4.2. A discussion of the mentioned results and study of the sensitivity to deviations from the Standard Model in the Higgs quartic interactions will occur in Section 5. We will also discuss potential improvements in this

section, followed by a review and conclusions in Section 6.

2 The theoretical framework and Monte Carlo simulation tools

The theoretical model description used here is based on the Standard Model with a modified Higgs potential to allow for deviations induced by new physics. The modification is introduced in a model-independent fashion,

$$V_h = \frac{1}{2}m_h^2 h^2 + \kappa_3 \lambda_{SM} v h^3 + \kappa_4 \frac{1}{4}\lambda_{SM} h^4, \tag{2.1}$$

namely in terms of otherwise free parameters, κ_3 and κ_4, as modification factors of trilinear and quartic scalar self-couplings (the SM is recovered for $\kappa_3 = \kappa_4 = 1$). In our notation, $m_h = 125$ GeV is the Higgs boson mass, v is the vacuum expectation value of the Higgs field, h denotes the physical Higgs-boson field, and λ_{SM} is the SM self-interaction coupling given by

$$\lambda_{SM} = \frac{m_h^2}{2v^2}. \tag{2.2}$$

To illustrate the role of the Higgs self-interactions, Figure 1 shows some of the Feynman diagrams contributing to triple Higgs production, together with their scaling with the coefficients κ_3 and κ_4. From the figure, it is clear that the production cross-section depends on both κ_3 and κ_4 parameters. In comparison, the double Higgs boson production depends only on κ_3. We should remark that large departures of κ_3 from the SM value are still allowed by current observations due to the lack of strong constraints as summarised in Ref. [19].

The introduction of the independent self-couplings approach does not necessarily represent a physically viable theory, but for our purposes, it can provide useful information about coupling sensitivity for SM-like triple Higgs boson production. This being said, it is beneficial to remark that the relation between the Higgs self-coupling and multi-Higgs production properties is only unambiguous in the SM. If we assume models Beyond the Standard Model, the multi-Higgs production rate could be altered by the presence of new BSM fields and interactions affecting the multi-Higgs production diagrams. These BSM effects could range from a modified top Yukawa coupling to higher-order Effective Field Theory (EFT) operators leading to new local vertices.

Signal and background processes are modeled using the simulated Monte Carlo (MC) event samples. These samples were produced with MG5aMC_2.6.7 version of MADGRAPH5_aMC@NLO [20]. The modified scalar potential described above was implemented into the existing UFO (Universal FeynRules Output) model called "loop_sm", provided by the MadGraph package, with UFO guidelines given in Ref. [21]. The "loop_sm" model contains both tree-level and loop-level information, necessary to produce the loop-induced triple Higgs signal. The decay of the produced Higgs bosons was provided by

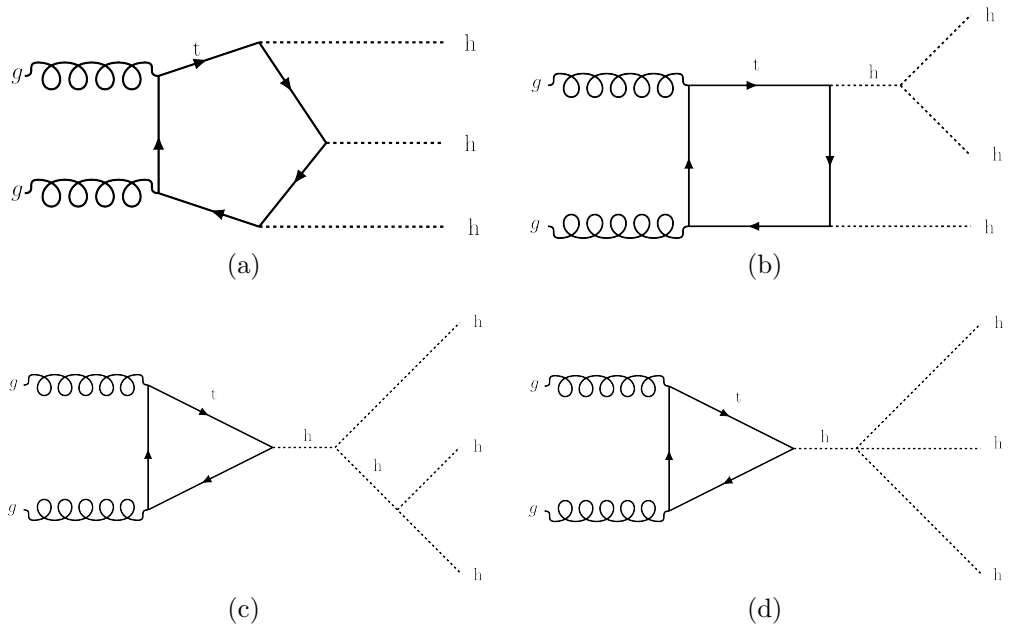

Figure 1: Feynman diagrams contributing to triple Higgs production via gluon fusion in the Standard Model. As described above, the corresponding matrix elements scaled by the coefficients κ_3 and κ_4 are as follows: (a) remains unmodified, (b) $\mathcal{M} \sim \kappa_3$, (c) $\mathcal{M} \sim \kappa_3^2$ and (d) $\mathcal{M} \sim \kappa_4$.

MadSpin [22]. To enable Higgs to decay into two photons[1], a direct vertex was implemented according to "heft" (Higgs Effective Field Theory) MadGraph model. The heft model uses "Infinite top mass approximation" (or "Infinite top mass limit")[2], which contracts the top quark and W-boson loop integral in the $H \to \gamma\gamma$ decay to an effective operator, used in tree-level diagram.

3 Event generation and analysis methods

The first stage of the study is to examine different processes contributing to triple Higgs production that may be used to show if and how it can be observed above the Standard Model background in a chosen channel. In Table 1, we have listed several triple Higgs boson production final states, with 30 ab^{-1} of integrated luminosity at a proton-proton collider at 100 TeV center-of-mass energy. The generation of the signal processes uses a four flavor scheme, i.e. in terms of four massless active quarks[3], and the model described in Section 2 and the MadGraph5_aMC@NLO framework. The events are generated at leading order

[1]The decay of the Higgs boson into two photons is a loop-induced process, which cannot be computed by MadGraph.

[2]Note that this approximation works only if the mass of the produced particles is smaller then mass of the top.

[3]A detailed description on 4-flavor or 5-flavor scheme can be found in Ref. [23]

(LO) using the subprocesses and gluon fusion with the full top mass dependence. The cross-sections of these processes are evaluated using the LO NN23LO1 (default setting) parton distribution functions.

As can be seen in Table 1, the dominant Higgs production mode is gluon fusion with subprocesses illustrated in Fig. 1, since, among other things, the gluons are the largest component of the protons *parton distribution functions* at high energies. The other known dominant Higgs production modes are vector-boson fusion, resulting in a signature of two high-rapidity jets that can be used to separate this process from the background. Other processes that provide a signal separation from the background are the gluon-gluon fusion plus two jets and the decay of W/Z boson to charged leptons or neutrinos for the triple Higgs–strahlung process (vector boson associated production). The last type of process of interest to consider is top associated production. In Figure 2, illustrating the cross-section calculations for main single-Higgs production mechanisms, we note that the rate of the sub-dominant modes (VBF h, $t\bar{t}h$ and Vh, where V stands for vector bosons $W^{\pm}, Z^0$) increases significantly from 8 TeV to 100 TeV of collision energy. In particular, the associated top pair production becomes as important as the vector boson fusion. A similar observation can be seen in our results, shown in Table 1. There is an exception to this, which is the vector-boson fusion mode represented by the green curve in Figure 2, and the same mode represented by the 6th row in Table 1 generated at LO tree-diagrams.

Production process	σ (ab)	Statistical error	$N(30\text{ab}^{-1})$
$gg \to hhh$	2060	8.70	61800
$pp \to hhhtb\ + j$	210	0.628	6302
$pp \to t\bar{t}hhh$	179	0.478	5380
$pp \to (W^+, W^-, Z)hhh$	38.5	0.115	1150
$pp > t\bar{t}t\bar{t}hhh$	1.19	1.42×10^{-2}	36
$pp \to jjhhh$	0.132	3.79×10^{-4}	4

Table 1: The LO total cross-section (at tree-level, except for $gg \to hhh$ which is a loop-induced process) and the number of events (rounded to the nearest integer) for several triple Higgs production channels at 100 TeV with 30 ab^{-1} of integrated luminosity with minimal generation cuts (for further details see below). The table consists of the following processes from the top: (1st) gluon-gluon fusion via quark loop-diagram, (2nd) single top associated production, (3rd) top pair associated production, (4th) vector boson associated production (or Higgs-strahlung process) from the fusion of a quark-anti-quark, (5th) 2 top pair associated production and (6th) vector-boson fusion (two quarks exchanging a $W^{\pm}$ or Z^0 boson that fuse to create Higgs bosons).

When considering the decay of the triple Higgs boson system, the most relevant channel in terms of branching ratios consists of a final state made of at least two jets originating from the fragmentation of b-quarks. Some of the decay modes, resulting in a number of events greater than 100 at 30 ab^{-1} of integrated luminosity from the gluon fusion process, are listed in Table 2. The task of separating the signal from the overwhelming pure QCD

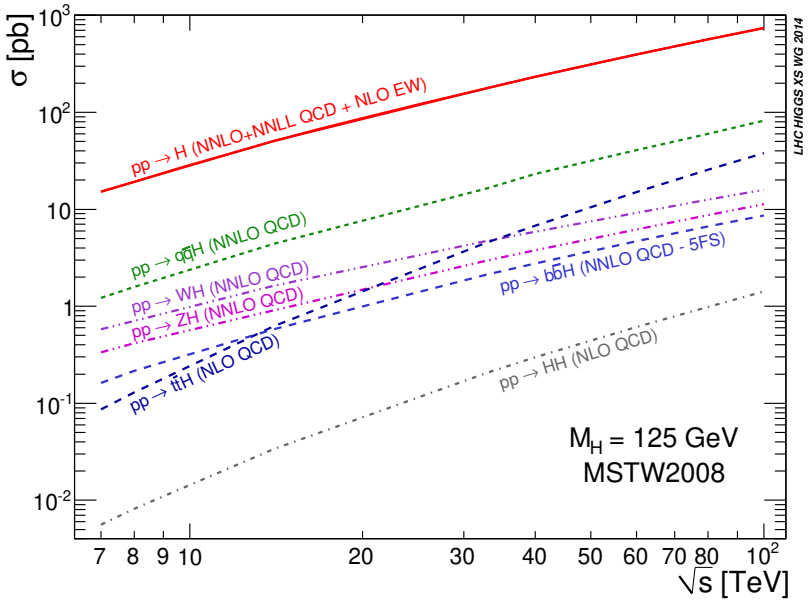

Figure 2: Higgs-boson production cross-sections as functions of centre-of-mass energy of pp collisions. This plot is taken from Ref. [24].

background, like for the $b\bar{b}b\bar{b}$ channel of the double Higgs-boson production, may not be possible without the use of either boosted object reconstruction techniques [25, 26, 27] or angular information [28]. Due to such techniques being strongly dependent on details of a future detector (such as tracking performance and calorimetric granularity), it is not easy to assess the usage of the six b-jet channel as a handle for separating the triple Higgs-boson signal from the background. Therefore, we leave the study of this channel as an open question and focus instead on analyzing the final state topologies that could be performed with any conceivable detector design. Since our goal is to ascertain if the triple Higgs production and by extension the quartic Higgs self-coupling is measurable, we apply the further requirement to omit the decay modes with neutrinos in the final states and to focus on processes that give more than than 100 events at 30 ab^{-1} of integrated luminosity.

With the imposed requirements described above, we are left with the following interesting final states: $(\tau\bar{\tau})(b\bar{b})(b\bar{b})$, $(\tau\bar{\tau})(\tau\bar{\tau})(b\bar{b})$, $(\gamma\gamma)(b\bar{b})(b\bar{b})$. The decay modes involving τ-leptons have distinct multi-lepton signatures as well as neutrinos in the final state, and the main background comes from non-prompt leptons. However, this decay mode receives a more severe background contamination compared to the $(\gamma\gamma)(b\bar{b})(b\bar{b})$ one. Another disadvantage is the neutrino production causing a loss of information, which affects the reconstruction of the Higgs bosons. Thus, to increase the likelihood of observation above the Standard Model background, the final state under consideration in our study contains two photons and four b-quarks having a clear resonant peak, at invariant mass equal to m_h. Therefore, the only Higgs production mode satisfying the above requirement of greater than 100 events is the gluon-gluon fusion. We make a note that the top quark associated

production contributes with around 26 events. To summarise, we determine the signal events as $(\gamma\gamma)(b\bar{b})(b\bar{b})$ events from triple Higgs production via gluon fusion. These are generated at LO, as higher-order corrections are not available for these loop-induced processes. It is worth to mention that QCD corrections are estimated to be large [29], and the sample could be normalized by a multiplicative K-factor of 2. However, such a factor has been omitted so that the results presented below can be seen as conservative.

$gg \to hhh \to$ final state	BR (%)	σ(ab)	$N(30\text{ab}^{-1})$
$(b\bar{b})(b\bar{b})(b\bar{b})$	19.2	396	11872
$(b\bar{b})(b\bar{b})(WW_{1l})$	7.204	148	4452
$(b\bar{b})(b\bar{b})(\tau\tau)$	6.312	130	3901
$(b\bar{b})(\tau\tau)(WW_{1l})$	1.578	32.5	975
$(b\bar{b})(b\bar{b})(WW_{2l})$	0.976	20.1	603
$(b\bar{b})(WW_{1l})(WW_{1l})$	0.901	18.6	557
$(b\bar{b})(\tau\tau)(\tau\tau)$	0.691	14.2	427
$(b\bar{b})(b\bar{b})(ZZ_{2l})$	0.331	6.82	205
$(b\bar{b})(WW_{2l})(WW_{1l})$	0.244	5.03	151
$(b\bar{b})(b\bar{b})(\gamma\gamma)$	0.228	4.70	141
$(b\bar{b})(\tau\tau)(WW_{2l})$	0.214	4.41	132
$(\tau\tau)(WW_{1l})(WW_{1l})$	0.099	2.04	61

Table 2: The list of channels for $N_{events} > 60$ with 30 ab^{-1} and their branching ratios (BR) from Ref. [30] (tables A1-A20). The subscript denotes the number of leptons in the final state, originating from the pair of gauge bosons. The cross-section is calculated at the LO for Higgs production via gluon-gluon fusion. The number of events has been rounded to the nearest integer.

It is important to note the approximations made when generating and calculating the different cross-sections for signal and background processes. Firstly, some of the processes are generated at LO tree-level; the implications of this are discussed in Section 5. Additionally, the width of the Higgs boson is set to zero (the width of the Higgs boson is very narrow compared to its mass), the decay of the Higgs boson into two photons relies on infinite top and W boson mass approximation. The branching ratio for $hhh \to \gamma\gamma b\bar{b}b\bar{b}$ has been rescaled to the corrected value with a multiplicative factor of 1.11 to reproduce the CERN's branching ratio calculation [31], which includes higher-order corrections in the Higgs boson decays. The decay of the signal events via Madspin was done with the spinmode setting set to none, as scalar particles induce no spin correlations. The documentation of MadGraph (and Madspin) syntax used in our implementation has been added into Appendix E.

The background processes for this specific decay channel can be classified when analyzing them at the parton level as resonant and non-resonant ones. The non-resonant background features the same final state as the signal process that is not associated with an intermediate resonance of the Higgs boson. These include for example prompt $\gamma\gamma b\bar{b}b\bar{b}$

(QCD) production, or a Z^0-boson decaying to $b\bar{b}$ pair. The resonant background contains the processes with one or two Higgs-resonant decays to the same final state particles as the signal, where the additional particles can be used as handles for discrimination. This is the case for instance of $hhb\bar{b}$, where $h \to b\bar{b}$ and $h \to \gamma\gamma$, as a background for the $hhh \to \gamma\gamma b\bar{b}b\bar{b}$ channel. All background processes considered in this study are listed in Table 3.

Process	σ (ab)	Statistical error	σ (ab)	MC error
$pp \to jjb\bar{b}b\bar{b}$	2.39×10^{12}	1.65×10^{10}	–	–
$pp \to \gamma jb\bar{b}b\bar{b}$	3.17×10^{9}	2.21×10^{7}	2.29×10^{3}	7.56×10^{-1}
$pp \to \gamma\gamma b\bar{b}jj$	7.61×10^{7}	4.29×10^{5}	2.30×10^{4}	47.4
$pp \to \gamma\gamma b\bar{b}b\bar{b}$	2.10×10^{6}	1.41×10^{4}	1.34×10^{-2}	3.44×10^{-3}
$pp \to \gamma\gamma t\bar{t}$	4.28×10^{5}	3.67×10^{3}	4.88×10^{2}	1.26
$pp \to \gamma\gamma Zjj$	1.38×10^{5}	783	35.8	4.62×10^{-2}
$pp \to hb\bar{b}b\bar{b}$	358	2.48	1.07×10^{-4}	1.49×10^{-7}
$pp \to hhZ$	264	2.40	5.23×10^{-5}	1.20×10^{-7}
$pp \to \gamma\gamma ZZ$	30.0	0.221	–	–
$pp \to hZZ$	0.949	2.17×10^{-3}	–	–
$pp \to hhjj$	4.80×10^{-2}	1.32×10^{-4}	2.61×10^{-2}	6.26×10^{-5}
$pp \to hhb\bar{b}$	2.68	0.119	–	–

Table 3: The total cross-section of the background processes for the $(b\bar{b})(b\bar{b})(\gamma\gamma)$ channel in pp collisions at 100 TeV. The background events were generated at tree-level, except for $pp \to hhb\bar{b}$ which was generated with loop-induced diagrams. The left cross-section column is events generated with minimal generation cuts and the right are with generation cuts given in the main text.

In order to maximize the Monte Carlo event efficiency in the signal region, we require all produced final-state particles at the generation level to have a transverse-momentum of $p_T > 20$ GeV for the jets and $p_T > 10$ GeV for the photons, a pseudorapidity satisfying $|\eta| < 5$ for the jets and $|\eta| < 2.5$ for the photons, and the invariant mass of a b-jet pair to be $|m_{b\bar{b}} - m_h| < 25$ GeV and $|m_{\gamma\gamma} - m_h| < 15$ for a photon pair. All particles are also required to be separated by an angular distance of $\Delta r = \sqrt{\Delta\eta^2 + \Delta\phi^2} > 0.4$. Background processes were generated at the tree level, with the exception of $pp \to hhb\bar{b}$ which was generated with loop-induced diagrams. Most of the background processes have large contributions from higher-order corrections. This is an issue that we will bring up in the discussion below.

As will become clear later on, our analysis will heavily depend on the identification and mistagging of b-jets. This is because the signal channel contains (parton-level) b-jets. We consider two b-tagging setups, with an efficiency of 70%, for a mistagging rate of a c-jet as a b-jet of 18% (1.8%) and a lighter jet as a b-jet of 1% (0.1%). These b-tagging performances were inspired by the ATLAS paper [32]. The misidentification rate of a jet as a photon is taken to be 0.1%. We inform the reader that the tagging rate is implemented at the selection stage, presented in Section 4.1.

There are some points in Table 3 that need to be addressed before moving on. We

observe that some of the processes lack values for the generation cuts, which we defined above. The processes involving two Z^0-bosons are generated on mass-shell and are evidently zero with the generation cuts. Specifically, the cut that eliminates them is $|m_{b_1 b_2} - m_h| < 15$ GeV. Decay of both Z^0-bosons on mass-shell can be argued as a good approximation since the likelihood of finding a Z^0 boson around the Higgs mass (which we are after) in the Z^0-mass distribution is very low, so consequently, we could neglect a contribution with ZZ. For the $pp \to jjb\bar{b}b\bar{b}$ process, we could estimate the contribution. With the tagging efficiency given above, we get $\sim 10^5$ ab. The lowest effect of the generation cuts is of order 10^{-3} on the non-resonant background, giving $\sim 10^2$ ab. If it behaves similar to $pp \to \gamma jb\bar{b}b\bar{b}$, one would obtain even lower contribution than for the $\gamma jb\bar{b}b\bar{b}$ process. Lastly, the $pp \to hhb\bar{b}$ process was not generated with the generation cuts as it was not needed to estimate the contribution to the background.

4 Phenomenological analysis

We perform a study of a triple-Higgs signal produced in proton-proton collisions at a center-of-mass energy of 100 TeV and show how it can be observed above the Standard Model background. The background events are generated with the generation cuts presented at the end of the previous section. We analyze final states comprised of four b-jets and a pair of photons. The investigation is divided into two parts: a rudimentary analysis of the events selection performance given in Section 4.1 and a phenomenological analysis of our process in Section 4.2.

4.1 Events selection

The differential cross-section analysis at a parton-level starts from determining a viable selection strategy. The observables used to exploit differences between the signal from the backgrounds are listed as follows:

- the transverse momentum of the leading and subleading photons, $p_T(\gamma_1)$ and $p_T(\gamma_2)$ respectively, and the p_T of the four b-tagged jets, $p_T(b_i)$ for $i = 1, 2, 3, 4$ (sorted by the decreasing values of their transverse momenta);

- the invariant mass of the diphoton and di-b-jet systems, $m_{\gamma_1\gamma_2}$, $m_{b_i b_j}$ for $i, j = 1, 2, 3, 4$ and $i \neq j$;

- the angular distance, in the $\eta - \phi$ plane, between the momentum of the diphoton system, $\Delta r(\gamma_1, \gamma_2)$, and for the di-$b$-jet system with the leading b-jet $\Delta r(b_1, b)$.

Additionally, each event was required to contain at least 4 b-tagged jets and 2 tagged photons. There were two other observables studied, the invariant mass of the 4 b system, $m_{b_1 b_2 b_3 b_4}$ and the azimuthal separation between the di-particle systems. The selection efficiency was deemed poor due to the non-negligible loss in signal events with respect to background events. The meaning of "non-negligible" refers to the fact that the signal

events have low statistics, and the rejection of these events has to be limited to estimate any signal sensitivity reliably. This point is illustrated in Figure 3, showing the number of remaining events as a function of the maximum $m_{b_1b_2b_3b_4}$ allowed, after applying the event selection strategy, which is presented below. One can see that the vertical distance (i.e., the relative number of events between the signal and background) diminishes only after signal events start to drop significantly.

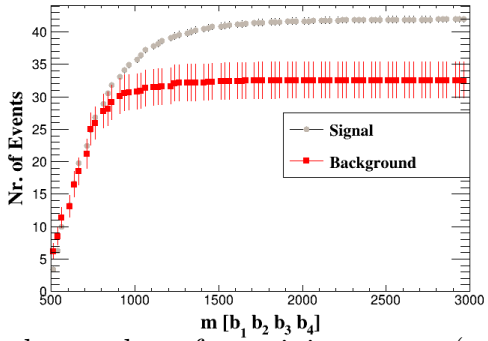

Figure 3: Plots illustrating the number of remaining events (calculated for a luminosity of 30 ab^{-1}) as a function of the invariant mass cut of the four b-tagged quarks (in GeV), after applying the event selection strategy.

It is important to note about the list of observables above regarding the reconstruction of the two Higgs candidates 4-momenta from the four b-tagged jets. For most b-jets, one cannot determine if the origin was a b-quark or an anti-b-quark. This gives us a 3-fold combinatorial ambiguity when trying to reconstruct our two Higgs candidates. This was solved by constructing the invariant masses of the four b-jets and imposing $|m_h - m_{bb_k}| < 15$ GeV for $k = 1, 2$. In the same manner as was done in Ref. [33], in case of several combinations of dijet systems fulfilling the criterion, we choose the dijet systems that minimize the mass asymmetry

$$\Delta_{bb_1,bb_2} = \frac{m_{bb_1} - m_{bb_2}}{m_{bb_1} + m_{bb_2}}.$$

The value of the selection cut was adopted from Ref. [34, 33], as it was for the invariant mass of the photons $|m_h - m_{\gamma\gamma}| < 5$ GeV.

The selection strategy was decided based on the plots of Figure 4 (and the distribution plots in Section 4.2, representing the number of signal and background events as a function of each consecutive (selection cut) variable used to separate the signal and background processes. Due to the constraint of low signal statistics, we require that the number of signal events rejected from the selection is limited to 3 events. The selection steps were chosen as follows. The events are required to contain at least four b-tagged jets, where jets can be misidentified as b-jets, and at least 2 tagged photons. The photons are required to possess transverse momenta $p_T(\gamma_{1,2}) > 55, 15$ GeV. The photon pairs are further required to have the invariant mass of $|m_h - m_{\gamma\gamma}| < 5$ GeV, as already mentioned. The angular distance Δr, in the $\eta - \phi$ plane, between the two photons is restricted to $\Delta r(\gamma_1, \gamma_2) < 3.6$. A similar

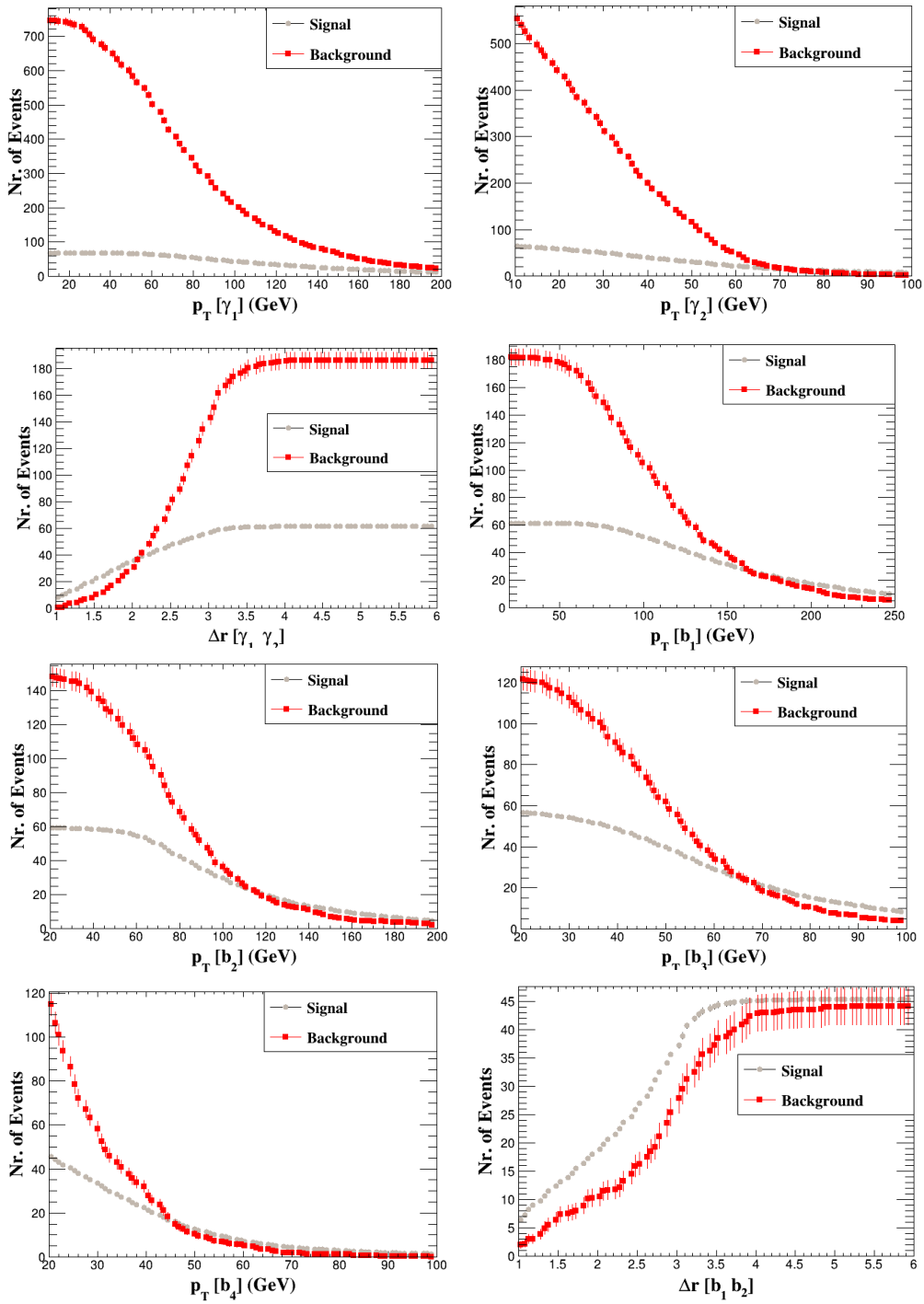

Figure 4: Plots illustrating the number of remaining events (calculated for a luminosity of 30 ab^{-1}) as a function of the cut on the selection variables after applying the previous selection steps summarized in Table 4.

strategy is then imposed on b-tagged jets. We required that the $p_T(b_i) > 75, 50, 20, 20$ GeV

for $i = 1, 2, 3, 4$, which denotes the hardest-p_T b-jets sorted in a decreasing order. The b-jets are then combined into two Higgs boson candidates by the manner described in the above paragraph. The last selection criteria were to limit the angular distance, in the $\eta - \phi$ plane, by $\Delta r(b_1, b) < 3.2$ between the leading b-jet and its partner in the Higgs candidate. We make the note that these selection cuts are compatible with the generation cuts. We summarize selection cuts in Table 4.

Selection step	Signal	$\gamma\gamma b\bar{b}b\bar{b}$	$\gamma\gamma b\bar{b}jj$	$\gamma\gamma t\bar{t}$	$\gamma\gamma Zjj$	$hhb\bar{b}$	$\gamma jb\bar{b}b\bar{b}$	S vs B
Initial	9.51	0.0268	45825	982	71.7	5.36	4580	0.230
Tagging	2.28	0.00642	22.2	0.0206	0.0488	1.46	1.10	2.40
$p_T(\gamma_1) > 55$ GeV	2.18	0.00642	16.6	0.0198	0.0427	1.27	0.523	2.62
$p_T(\gamma_2) > 15$ GeV	2.05	0.00642	14.8	0.0190	0.0377	1.22	0.422	2.60
$\lvert m_{\gamma_1\gamma_2} - m_h \rvert < 5$ GeV	2.05	0.00214	4.94	0.0167	0.0153	1.22	0.0152	3.90
$\Delta r(\gamma_1\gamma_2) < 3.6$	2.04	0.00214	4.81	0.0167	0.0152	1.21	0.0124	3.93
$p_T(b_1) > 75$ GeV	1.97	0.00214	4.09	0.0142	0.0117	0.840	0.00968	4.10
$p_T(b_2) > 50$ GeV	1.92	0.00214	3.65	0.0125	0.0106	0.472	0.00968	4.26
$p_T(b_3) > 20$ GeV	1.89	0.00214	3.65	0.0125	0.0106	0.363	0.00968	4.25
$p_T(b_4) > 20$ GeV	1.52	0.00214	3.65	0.0125	0.0106	0.132	0.00968	3.59
$\lvert m_{b_i,b_j} - m_h \rvert < 15$ GeV	1.52	0.00214	1.44	0.00127	0.00331	0.0173	0.00830	4.80
$\Delta r(b_1, b_2) < 3.2$	1.51	0.00107	1.42	0.00126	0.00326	0.0150	0.00692	4.80

Table 4: Effects of our selection strategy on the SM signal and background with generation cuts. We present the resulting cross-sections (ab) after each of the selection steps, together with the related signal significance "S vs B", defined as $S/\sqrt{(S+B)}$, where S and B are the number of events for the signal and background, respectively. The significance has been calculated for a luminosity of 30 ab^{-1}. In the table, we assume a b-tagging efficiency of 70% and a mistagging rate of c and lighter jets as a b-jet of 18% and 1%, respectively. The misidentification rate of jets as photons is 0.1%.

Together with the event selection strategy, we summarize its effectiveness in Table 4. The background processes of the resonant type, $hb\bar{b}b\bar{b}$, hhZ and $hhjj$, have a negligible contribution and are instead listed in Appendix A. This low cross-section is a result of just considering tree-level diagrams and excluding higher-order corrections. As we mentioned earlier, we will discuss and estimate their contribution in Section 5.

The b-tagging strategy is the most dominant factor in the prospect of distinguishing the signal from the background. This can be seen in the "Tagging" selection step. In the next section, we will see the effect of the choice of the b-mistagging set. There is a deviation from our expectation of the selection strategy shown in Table 4 that is needed to be pointed out. It occurs at the $p_T(b_4) > 20$ GeV selection step. We see that only the signal is significantly affected by the selection. This has to do with the cuts at the generation level, where the background processes are already required to have $p_T(b) > 20$ GeV, while the final-state

particles for the signal event were generated with Madspin without generation cuts.

4.2 Differential distributions

In this sub-section, we present the differential distributions in triple Higgs production with its dominant background, the $\gamma\gamma b\bar{b}jj$ process, in the Standard Model. The signal is presented with different values for the quartic scalar self-couplings, where the Standard Model is recovered for $\kappa_4 = 1$. With minimal generation cuts, we get the following cross-section by varying the quartic self-coupling while keeping the SM value for the cubic self-coupling ($\kappa_3 = 1$):

$$\sigma(\kappa_4 = -1, 0, 1, 2, 4) \times 10^{-3} = 2.75, 2.37, 2.06, 1.83, 1.61 \text{ ab}.$$

The event selection (summarized in Table 4) has been applied to each plot.

Before moving to differential distributions, one can comment on the previous cross-section dependence on κ_4. The fact that the dependence does not yield a significant overall change in cross-section motivates us to look to the differential distributions and see if there is some phase-space dependence that could help to disentangle various κ_4 values. To show this dependence, we present a BSM-to-SM ratio times $\sigma_{\text{SM}}/\sigma_{\text{BSM}}$ (the latter factor removes the overall change due to cross-section), with each distribution. The ratio for the $\kappa_4 = 2$ signal is not present in these plots, but is instead provided in Appendix B. This makes the plots more readable, while $\kappa_4 = 2$ does not provide any additional new information to our discussion. Taking a look at each ratio, we can observe some phase-space dependence, which for the most part lies within a factor of 0.5-1.5. One can make an observation that the size of the deviation from the SM is proportional to the change of κ_4, by comparing the case of $\kappa_4 = 4$ to the rest.

Figure 5 shows the transverse momentum of the leading photon, $p_T(\gamma_1)$. The transverse momenta of the sub-leading and the b-tagged jets are qualitatively similar and can be found in Appendix C. Evidently, the corresponding distribution for the background $\gamma\gamma b\bar{b}jj$ is of the same order of magnitude for $p_T \lesssim 200$ GeV, and peaking at a similar value. The tail of the p_T distribution for the $\gamma\gamma b\bar{b}jj$ process becomes much smaller than that of the signal, see the left logarithmic-scale plot for $p_T \gtrsim 200$ GeV.

We examine the invariant-mass distribution of the four leading b-jets system in Figure 6. For this observable, one finds it difficult to see a difference between the signal and the $\gamma\gamma b\bar{b}jj$ background.

In Figure 7, we show the spectrum of the azimuthal separation (right) and the angular distance (left), in the $(\eta - \phi)$ plane, of the diphoton system (top) and the di-b-jet "system" for the leading b-jet pair. One can observe that in the case of the photons, the $\gamma\gamma b\bar{b}jj$ events generally have higher separation than the diphotons resulting from the Higgs boson decay, as expected. The same correlation is not present for the separation of the b-jets, making it harder to separate the $\gamma\gamma b\bar{b}jj$ from the signal.

The results of the second mistagging weight set (c as b-jets 1.8% and lighter jets as a b-jet 0.1%) are presented in Appendix D in the form of plots corresponding to those

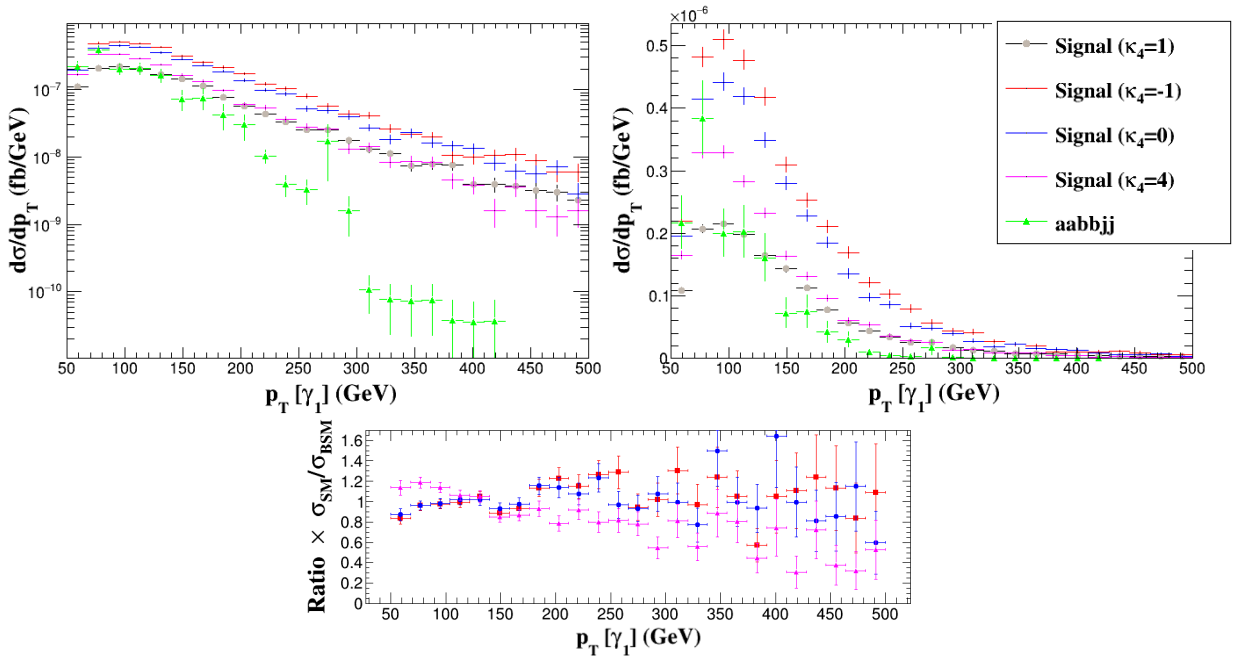

Figure 5: Transverse momentum distribution of the leading photon for the triple-Higgs signal and the $\gamma\gamma b\bar{b}jj$ background (log-scale plot on the upper left) plot. The signal is plotted with different values for the quartic scalar self-coupling, κ_4 (SM for $\kappa_4 = 1$). The plot below represent a BSM-to-SM ratio times $\sigma_{\rm SM}/\sigma_{\rm BSM}$ of the above distribution plot.

given in this section. Note, the information contained in those plots is already present in the figures given in this section. We summarized the differences in Table 5. The only visual difference (omitting the transformation into log-scale) is an overall normalization of the curve directly proportional to the changed mistagging weights (a factor 1/10) for the participating particles it concerns to. There is one exception, and that is the $\gamma\gamma t\bar{t}$ process. However, showing these plots and table is still of interest because it "reveals" the signal on top of the background. Besides, it also shows the importance of high level b-tagging efficiencies and low level misidentifications for a future collider if we want to target such processes and to measure the quantities like the κ_4. This will be further discussed in Section 5.

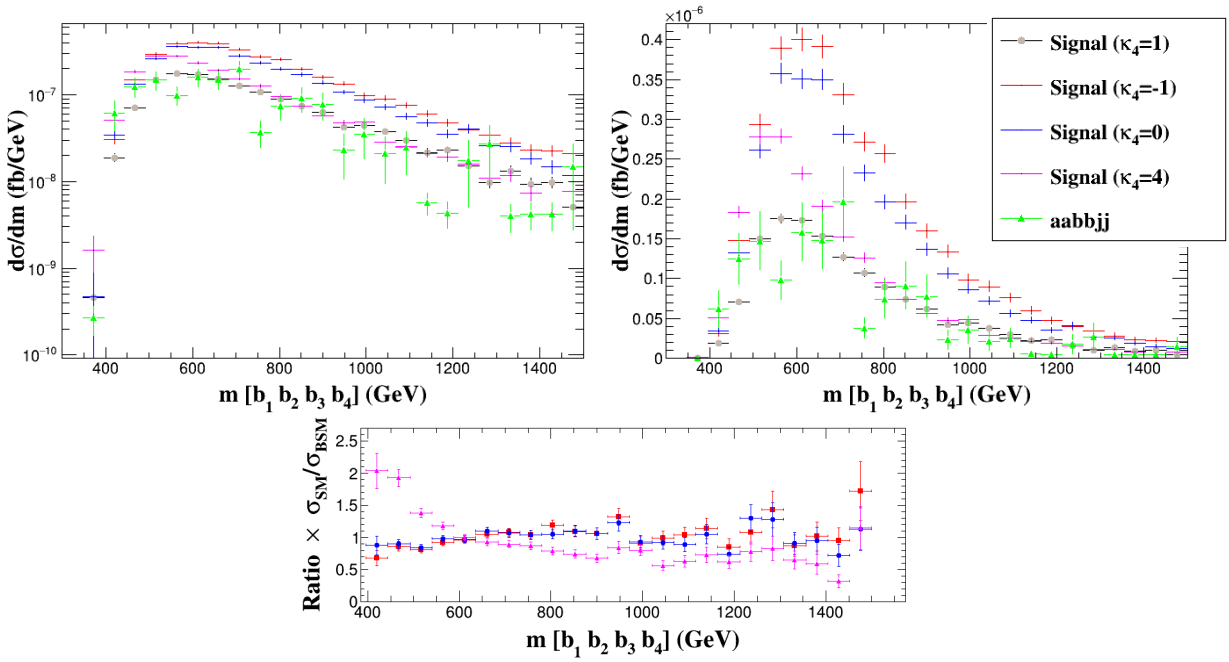

Figure 6: Invariant-mass distributions of the four leading b-tagged jets (log-scale plot on the upper left) plot for the triple-Higgs signal and the $\gamma\gamma b\bar{b}jj$ background. The signal is plotted with different values for the quartic scalar self-coupling, κ_4 (SM for $\kappa_4 = 1$). The plot below represents a BSM-to-SM ratio times $\sigma_{\rm SM}/\sigma_{\rm BSM}$ of the above distribution plot.

	Signal	$\gamma\gamma b\bar{b}b\bar{b}$	$\gamma\gamma b\bar{b}jj$	$\gamma\gamma t\bar{t}$	$\gamma\gamma Zjj$	$hhbb$
σ (ab)	1.51	0.00107	0.0142	8.51×10^{-5}	3.26×10^{-5}	0.0151
	$\gamma j b\bar{b}b\bar{b}$	hhZ	$hhjj$	$hb\bar{b}b\bar{b}$	S vs B	
σ (ab)	0.00692	1.53×10^{-5}	3.92×10^{-7}	3.04×10^{-5}	6.64	

Table 5: The resulting cross-sections (ab) with the event selection applied, together with the related signal significance "S vs B", defined as $S/\sqrt{(S+B)}$, where S and B are the number of events for the signal and background, respectively. The significance has been calculated for a luminosity of 30 ab^{-1}. The second set of mistagging rates is used, where $c \to b$ is 1.8% and lighter jets as a b-jet is of 0.1%.

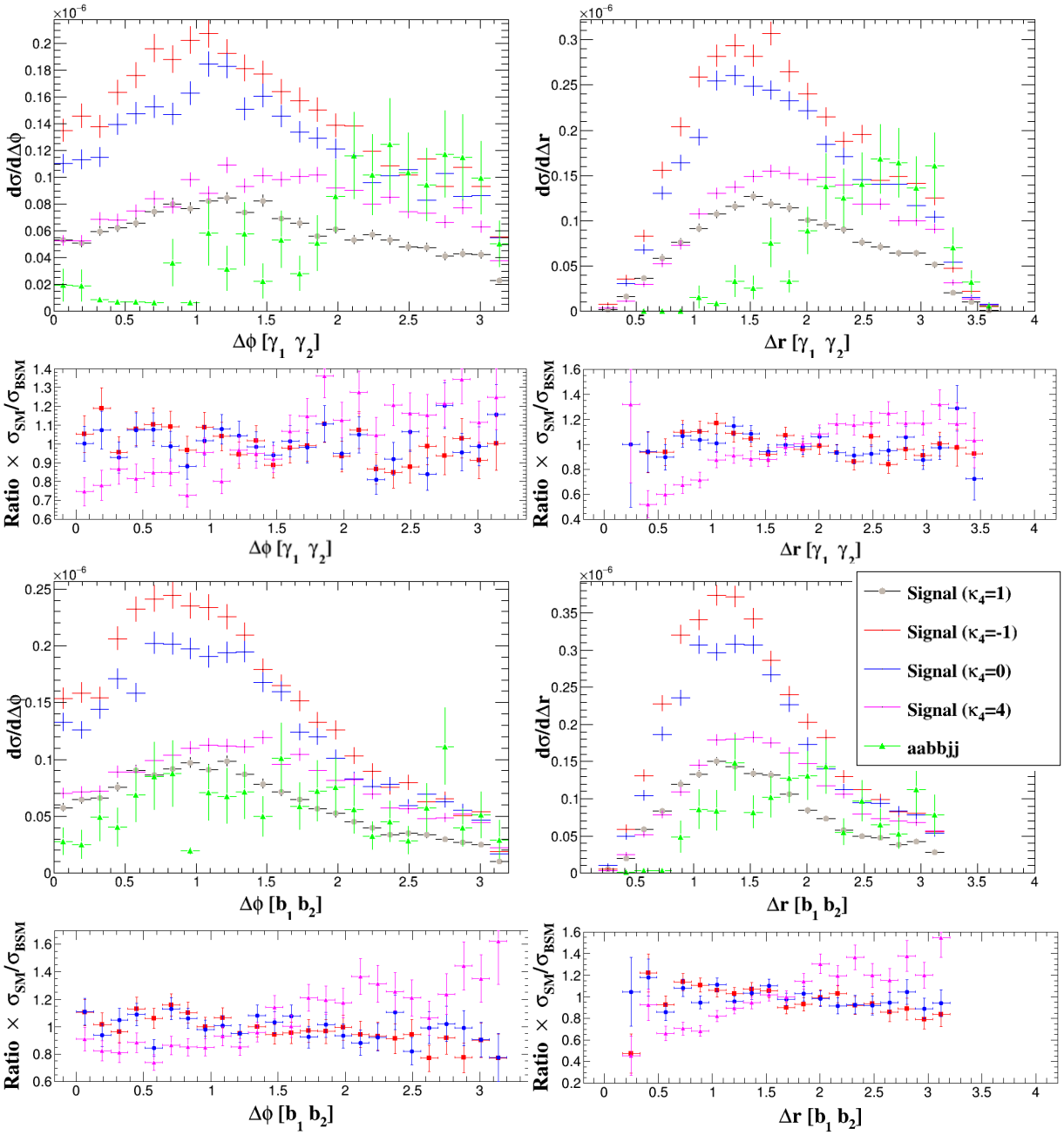

Figure 7: Azimuthal separation (right) and angular distance (left), in $(\eta - \phi)$ plane, distributions of diphoton system (the above plots) and di-b-tagged jets (the below plots) for the triple-Higgs signal and the $\gamma\gamma b\bar{b}jj$ background. The signal is plotted with different values for the quartic scalar self-coupling, κ_4 (SM for $\kappa_4 = 1$). The plots below each distribution plot represent the corresponding BSM-to-SM ratio times $\sigma_{\rm SM}/\sigma_{\rm BSM}$.

5 Discussion

We start the discussion by reminding the reader that the resonant background is generated at tree-level. We expect both loop-induced contributions and higher-order corrections to be important for the background, which we can see by comparing the ratio of our estimations of $pp \to hhb\bar{b}$ (with loop-induced diagrams) and $pp \to hhjj$ (without loop-induced diagrams) cross-sections, with that for $pp \to q\bar{q}h$ and $pp \to b\bar{b}h$ processes in Figure 2. The difference is a factor of 1000. We can try to estimate the size of these processes by extrapolating from what we have presented so far and try to predict their significance. From Figure 2, we see that the cross-section increases by a factor of $\mathcal{O}(10)$ going from $pp \to hb\bar{b}$ to $pp \to hq\bar{q}$. Similarly from Table 3, we see that the difference between $pp \to \gamma\gamma b\bar{b}b\bar{b}$ and $pp \to \gamma\gamma b\bar{b}jj$ is of order $\mathcal{O}(10)$. One could guess that the relation between our calculated $pp \to hhb\bar{b}$ process and $pp \to hhjj$ would be of a similar magnitude. Since the resonant background processes are less reducible by the event selection, due to having few particles that can be used as handles for separating the background from the signal, one can say that $pp \to hhjj$ would be an important process contributing to the background. On the other hand, the $hhjj$ will suffer from the jet-to-b efficiency factors twice. Less significant contribution can be found from the $pp \to hhZ$ process, as the invariant mass of the decay product of the Z-boson is unlikely to be at the mass of the Higgs boson. The $pp \to hb\bar{b}b\bar{b}$ process is harder to estimate as we have no similar process with a single Higgs boson production from loop diagram to compare with. Nevertheless, to properly identify and quantify relevant background processes and determine an effective strategy of separating them from the signal, one would need to take into account higher-order corrections and loop-induced diagrams for the background processes and the signal. However, as mentioned earlier, the signal process was estimated to be large, while the higher-order corrections are unknown.

A way of limiting the number of uncertainties would be to take into account detector effects. As mentioned before, due to the unknown specifications of the future collider and a limited time frame, this was not included in this thesis. However, one could include simplistic detector effects based on existing detector performances and smear the momentum and energy of the produced photons and jets according to the value of their transverse momenta. This would give us a more reliable quantitative result, including a reasonable expectation of uncertainty.

Returning to our results in the previous section, we chose two b-tagging setups with the efficiency of 70% and the related mistagging rates of a c-jet (light jet) to b-jet of 18% (1%) and 1.8% (0.1%). One can observe that to have a reasonably clear signal, the detector of an FCC-hh needs to have a good c-jet and light jet rejection rate of $\mathcal{O}(1\%)$ over a wide phase space range. Another important note to make is the sensitivity of the signal to the b-tagging efficiency. As the signal has low statistics, a "small" reduction from 80% to 70% would imply a loss of $\approx 40\%$ due to the reconstruction of the four b-jets.

Another part of our results was optimizing the event selection strategy. It was done by finding appropriate event selection cuts to minimize the background events in reference to the signal events while keeping the loss of valuable signal events low. We use the classic

approach by assuming that the measured quantities in the event do not vary with other quantities in the event. While easy to implement, making the cuts can be an arbitrary and inexact procedure, where we most probably do not make optimal use of the information available in the event. A better way of performing this would be in a multi-variable sense, but the space of all possible cuts on just a few event quantities is huge. This would take care of hidden correlations between our quantities. A common solution to this is the use of neural networks. However, in the view of available time, this has been left for future studies. This is because the training of a neural network usually time consuming as it takes large samples of signal and background to obtain stable results, and tends to converge logarithmically.

In conclusion, we have shown that the study of triple Higgs production for future collider program has a good potential but is a challenging task. Our analysis of the $\gamma\gamma b\bar{b}b\bar{b}$ channel has shown promising results for measuring and constraining the Higgs quartic self-coupling relevant for exploring the electroweak symmetry breaking and BSM physics. Though our analysis was a baseline study, it definitely prompts for further investigation.

6 Conclusions

We have studied the prospects for measuring the triple Higgs boson production at the future circular proton-proton collider with a center-of-mass energy of 100 TeV, in the case when the three Higgs bosons decay to the $\gamma\gamma b\bar{b}b\bar{b}$ final state. This investigation was done by constructing a phenomenological LO parton-level analysis. In this analysis, the three Higgs bosons were produced in a Standard Model-like fashion, where we allowed for independent variation of the quartic self-coupling. We show the efficiency of a selection strategy and demonstrate a heavy dependence of the signal significance on the tagging efficiencies. Furthermore, we obtain a signal significance of $S/\sqrt{S+B} \approx 5$ and observe phase space regions where the signal is relatively clean. We conclude that the $\gamma\gamma b\bar{b}b\bar{b}$ final state is an important candidate for the study of the self-couplings of the Higgs boson in the Standard Model and beyond.

Concerning further research, the first step is to cover the absence of higher-order calculations and dominating loop-induced diagrams for several background processes. A more detailed analysis should include detector effects, as the current results are based on an existing detector performance and smearing of the produced particles' momenta and energies according to the value of their transverse momenta. One could also improve upon the event selection with advanced multivariate techniques, leading to higher signal significance. However, we have shown with a simple baseline analysis that there is a strong potential for further studies of triple Higgs boson production as a promising way to constrain the quartic Higgs self-coupling at a future 100 TeV hadron collider.

References

[1] **ATLAS** Collaboration, G. Aad *et al.*, "Observation of a new particle in the search for the Standard Model Higgs boson with the ATLAS detector at the LHC," *Phys. Lett. B* **716** (2012) 1–29, arXiv:1207.7214 [hep-ex].

[2] **CMS** Collaboration, S. Chatrchyan *et al.*, "Observation of a New Boson at a Mass of 125 GeV with the CMS Experiment at the LHC," *Phys. Lett. B* **716** (2012) 30–61, arXiv:1207.7235 [hep-ex].

[3] **CMS** Collaboration, S. Chatrchyan *et al.*, "Observation of a New Boson at a Mass of 125 GeV with the CMS Experiment at the LHC," *Phys. Lett.* **B716** (2012) 30–61, arXiv:1207.7235 [hep-ex].

[4] "LEP/TEV EW WG Plots for Summer." http://lepewwg.web.cern.ch/LEPEWWG/plots/summer2010/, 2010. [Online; accessed 6-February-2020].

[5] A. J. Long, *The Electroweak Phase Transition: Corralling the Higgs with Colliders & Cosmology*. PhD thesis, Wisconsin U., Madison, 2012. http://dark.ft.uam.es/mununiverse/images/tesis$_a$*ndrew.pdf*.

[6] M. Carena and C. E. M. Wagner, "Electroweak baryogenesis and Higgs physics," arXiv:hep-ph/9704347 [hep-ph].

[7] M. Reichert, A. Eichhorn, H. Gies, J. M. Pawlowski, T. Plehn, and M. M. Scherer, "Probing baryogenesis through the Higgs boson self-coupling," *Phys. Rev.* **D97** no. 7, (2018) 075008, arXiv:1711.00019 [hep-ph].

[8] S. Dawson *et al.*, "Working Group Report: Higgs Boson," in *Proceedings, 2013 Community Summer Study on the Future of U.S. Particle Physics: Snowmass on the Mississippi (CSS2013): Minneapolis, MN, USA, July 29-August 6, 2013*. 2013. arXiv:1310.8361 [hep-ex].

[9] R. Frederix, S. Frixione, V. Hirschi, F. Maltoni, O. Mattelaer, P. Torrielli, E. Vryonidou, and M. Zaro, "Higgs pair production at the LHC with NLO and parton-shower effects," *Phys. Lett.* **B732** (2014) 142–149, arXiv:1401.7340 [hep-ph].

[10] U. Baur, T. Plehn, and D. L. Rainwater, "Probing the Higgs selfcoupling at hadron colliders using rare decays," *Phys. Rev.* **D69** (2004) 053004, arXiv:hep-ph/0310056 [hep-ph].

[11] T. Plehn, M. Spira, and P. M. Zerwas, "Pair production of neutral Higgs particles in gluon-gluon collisions," *Nucl. Phys.* **B479** (1996) 46–64, arXiv:hep-ph/9603205 [hep-ph]. [Erratum: Nucl. Phys.B531,655(1998)].

[12] T. Plehn and M. Rauch, "The quartic higgs coupling at hadron colliders," *Phys. Rev.* **D72** (2005) 053008, arXiv:hep-ph/0507321 [hep-ph].

[13] F. Boudjema and E. Chopin, "Double Higgs production at the linear colliders and the probing of the Higgs selfcoupling," *Z. Phys.* **C73** (1996) 85–110, arXiv:hep-ph/9507396 [hep-ph].

[14] A. J. Barr, M. J. Dolan, C. Englert, and M. Spannowsky, "Di-Higgs final states augMT2ed – selecting hh events at the high luminosity LHC," *Phys. Lett.* **B728** (2014) 308–313, arXiv:1309.6318 [hep-ph].

[15] Q. Li, Q.-S. Yan, and X. Zhao, "Higgs Pair Production: Improved Description by Matrix Element Matching," *Phys. Rev.* **D89** no. 3, (2014) 033015, arXiv:1312.3830 [hep-ph].

[16] F. Goertz, A. Papaefstathiou, L. L. Yang, and J. Zurita, "Higgs Boson self-coupling measurements using ratios of cross sections," *JHEP* **06** (2013) 016, arXiv:1301.3492 [hep-ph].

[17] M. Cepeda *et al.*, "Report from Working Group 2: Higgs Physics at the HL-LHC and HE-LHC," *CERN Yellow Rep. Monogr.* **7** (2019) 221–584, arXiv:1902.00134 [hep-ph].

[18] M. L. Mangano *et al.*, "Physics at a 100 TeV pp Collider: Standard Model Processes," *CERN Yellow Rep.* no. 3, (2017) 1–254, arXiv:1607.01831 [hep-ph].

[19] **Particle Data Group** Collaboration, M. e. a. Tanabashi, "Review of particle physics," *Phys. Rev. D* **98** (Dec, 2019) 030001. https://pdg.lbl.gov/2019/reviews/rpp2018-rev-higgs-boson.pdf.

[20] J. Alwall, R. Frederix, S. Frixione, V. Hirschi, F. Maltoni, O. Mattelaer, H. S. Shao, T. Stelzer, P. Torrielli, and M. Zaro, "The automated computation of tree-level and next-to-leading order differential cross sections, and their matching to parton shower simulations," *JHEP* **07** (2014) 079, arXiv:1405.0301 [hep-ph].

[21] C. Degrande, C. Duhr, B. Fuks, D. Grellscheid, O. Mattelaer, and T. Reiter, "UFO - The Universal FeynRules Output," *Comput. Phys. Commun.* **183** (2012) 1201–1214, arXiv:1108.2040 [hep-ph].

[22] P. Artoisenet, R. Frederix, O. Mattelaer, and R. Rietkerk, "Automatic spin-entangled decays of heavy resonances in Monte Carlo simulations," *JHEP* **03** (2013) 015, arXiv:1212.3460 [hep-ph].

[23] F. Maltoni, G. Ridolfi, and M. Ubiali, "b-initiated processes at the LHC: a reappraisal," *JHEP* **07** (2012) 022, arXiv:1203.6393 [hep-ph]. [Erratum: JHEP 04, 095 (2013)].

[24] "Higgs cross sections for European Strategy studies in 2012." https://twiki.cern.ch/twiki/bin/view/LHCPhysics/HiggsEuropeanStrategy2012.

[25] D. Wardrope, E. Jansen, N. Konstantinidis, B. Cooper, R. Falla, and N. Norjoharuddeen, "Non-resonant higgs pair production in the $b\bar{b}b\bar{b}$ final state at the lhc," 2014.

[26] D. E. F. de Lima, A. Papaefstathiou, and M. Spannowsky, "Standard model higgs boson pair production in the $(b\bar{b})(b\bar{b})$ final state," 2014.

[27] B. Cooper, N. Konstantinidis, L. Lambourne, and D. Wardrope, "Boosted $hh \to b\bar{b}b\bar{b}$: a new topology in searches for tev-scale resonances at the lhc," 2013.

[28] M. J. Dolan, C. Englert, and M. Spannowsky, "Higgs self-coupling measurements at the lhc," 2012.

[29] F. Maltoni, E. Vryonidou, and M. Zaro, "Top-quark mass effects in double and triple Higgs production in gluon-gluon fusion at NLO," *JHEP* **11** (2014) 079, `arXiv:1408.6542 [hep-ph]`.

[30] S. Dittmaier *et al.*, "Handbook of LHC Higgs Cross Sections: 2. Differential Distributions," `arXiv:1201.3084 [hep-ph]`.

[31] R. Tanaka, "Sm higgs branching ratios and total decay widths (update in cern report4 2016)," Mar, 2016. https://twiki.cern.ch/twiki/bin/view/LHCPhysics/CERNYellowReportPageBR.

[32] **ATLAS Collaboration** Collaboration, "b-tagging in dense environments," Tech. Rep. ATL-PHYS-PUB-2014-014, CERN, Geneva, Aug, 2014. https://cds.cern.ch/record/1750682.

[33] B. Fuks, J. H. Kim, and S. J. Lee, "Probing higgs boson self-interactions in proton-proton collisions at a center-of-mass energy of 100 tev," *Physical Review D* **93** no. 3, (Feb, 2016) . http://dx.doi.org/10.1103/PhysRevD.93.035026.

[34] D. Wardrope, E. Jansen, N. Konstantinidis, B. Cooper, R. Falla, and N. Norjoharuddeen, "Non-resonant higgs-pair production in the $b\bar{b}b\bar{b}$ final state at the lhc," *The European Physical Journal C* **75** no. 5, (May, 2015) . http://dx.doi.org/10.1140/epjc/s10052-015-3439-0.

A Event selection for the resonant background process

Selection step	hhZ	$hhjj$	$hbbbb$
Initial	1.05×10^{-4}	0.0522	2.15×10^{-4}
At least 4 b	2.51×10^{-5}	1.14×10^{-4}	5.16×10^{-5}
$p_T(\gamma_1) > 55$ GeV	2.41×10^{-5}	1.06×10^{-4}	4.89×10^{-5}
$p_T(\gamma_2) > 15$ GeV	2.36×10^{-5}	1.05×10^{-4}	4.76×10^{-5}
$M(\gamma_1, \gamma_2) < 5$ GeV	2.36×10^{-5}	1.05×10^{-4}	4.76×10^{-5}
$\Delta r(\gamma_1, \gamma_2) < 3.6$	2.35×10^{-5}	1.04×10^{-4}	4.75×10^{-5}
$p_T(b_1) > 75$ GeV	2.16×10^{-5}	7.94×10^{-5}	4.37×10^{-5}
$p_T(b_2) > 50$ GeV	2.16×10^{-5}	6.42×10^{-5}	4.35×10^{-5}
$p_T(b_3) > 20$ GeV	2.16×10^{-5}	6.42×10^{-5}	4.35×10^{-5}
$p_T(b_4) > 20$ GeV	2.16×10^{-5}	6.42×10^{-5}	4.35×10^{-5}
$M(b_i, b_j) < 15$ GeV	1.54×10^{-5}	4.03×10^{-5}	3.14×10^{-5}
$\Delta r(b_1, b_2) < 3.2$	1.53×10^{-5}	3.92×10^{-5}	3.04×10^{-5}

Table 6: Effects of our selection strategy on the SM signal and background. We present the resulting cross-sections after each of the selection steps. In the table, we assume a b-tagging efficiency of 70% and a mistagging rate of c and lighter jets as a b-jet of 18% and 1%, respectively.

B BSM-to-SM ratio distributions

We show in Figure 8 the ratio distributions presented in Section 4.2, together with $\kappa_4 = 2$ case.

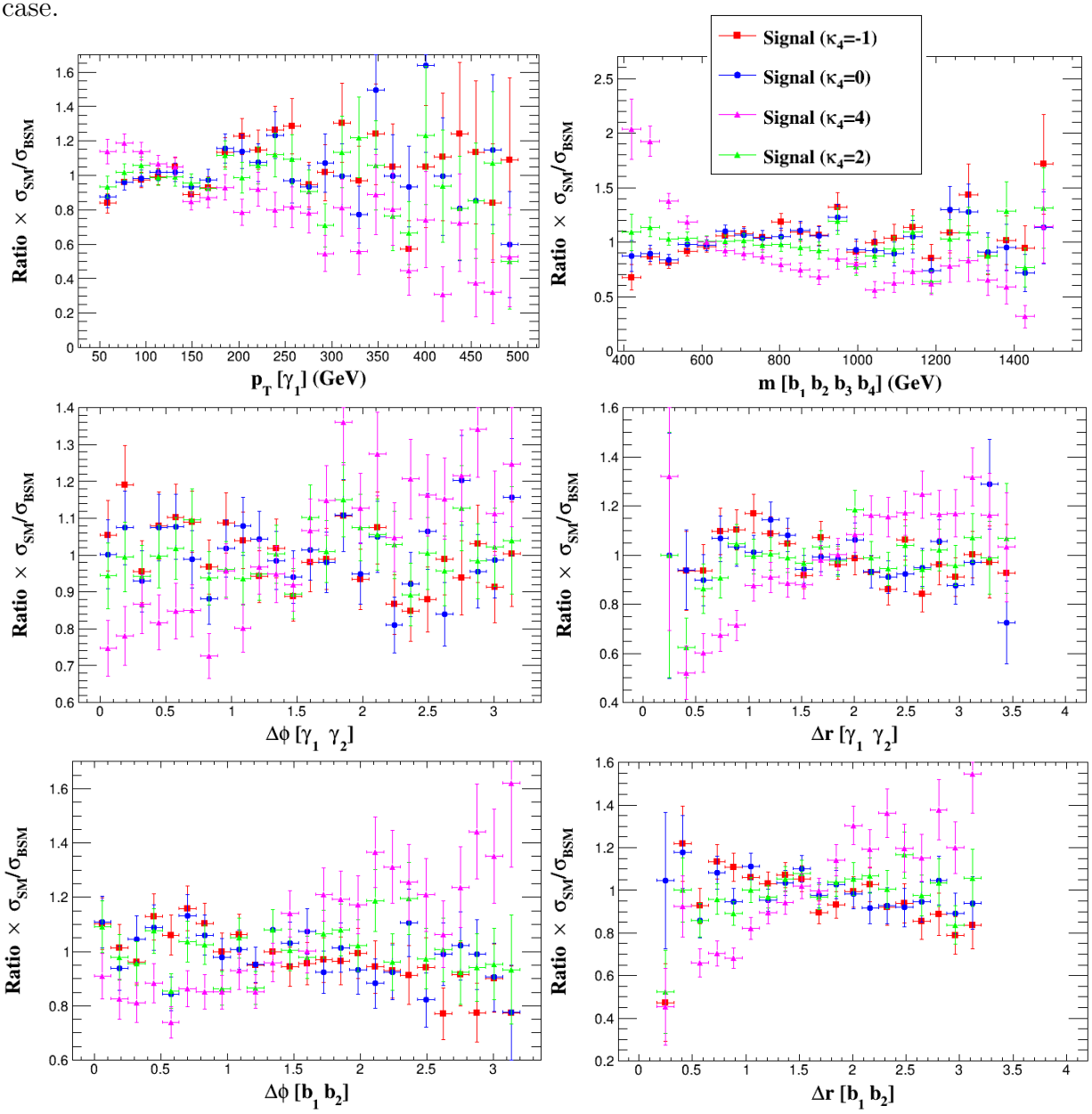

Figure 8: The BSM-to-SM ratio times $\sigma_{\rm SM}/\sigma_{\rm BSM}$ distribution plots for the observables under consideration in Section 4.2, together with $\kappa_4 = 2$ case. The signal is plotted for different values of the quartic scalar self-coupling, κ_4 (SM for $\kappa_4 = 1$).

C Transverse momentum distribution

In this section, we show the transverse momentum distributions for sub-leading photon and the four leading b-jets. These contain similar information to that of the transverse momentum distributions for the leading photon, shown in Section 4.2.

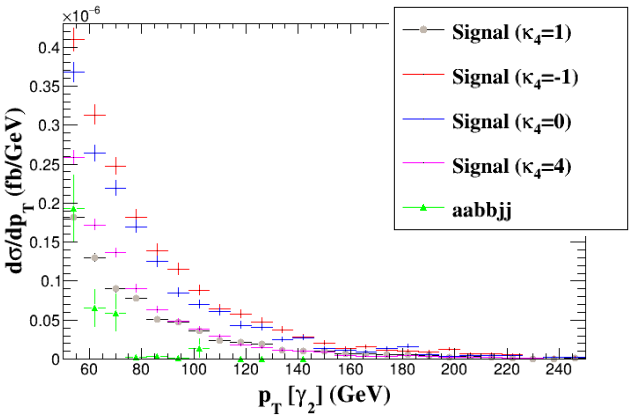

Figure 9: Transverse momentum distribution of the sub-leading photon for the triple-Higgs signal and the $\gamma\gamma b\bar{b}jj$ background. The signal is plotted for different values of the quartic scalar self-coupling, κ_4 (SM for $\kappa_4 = 1$).

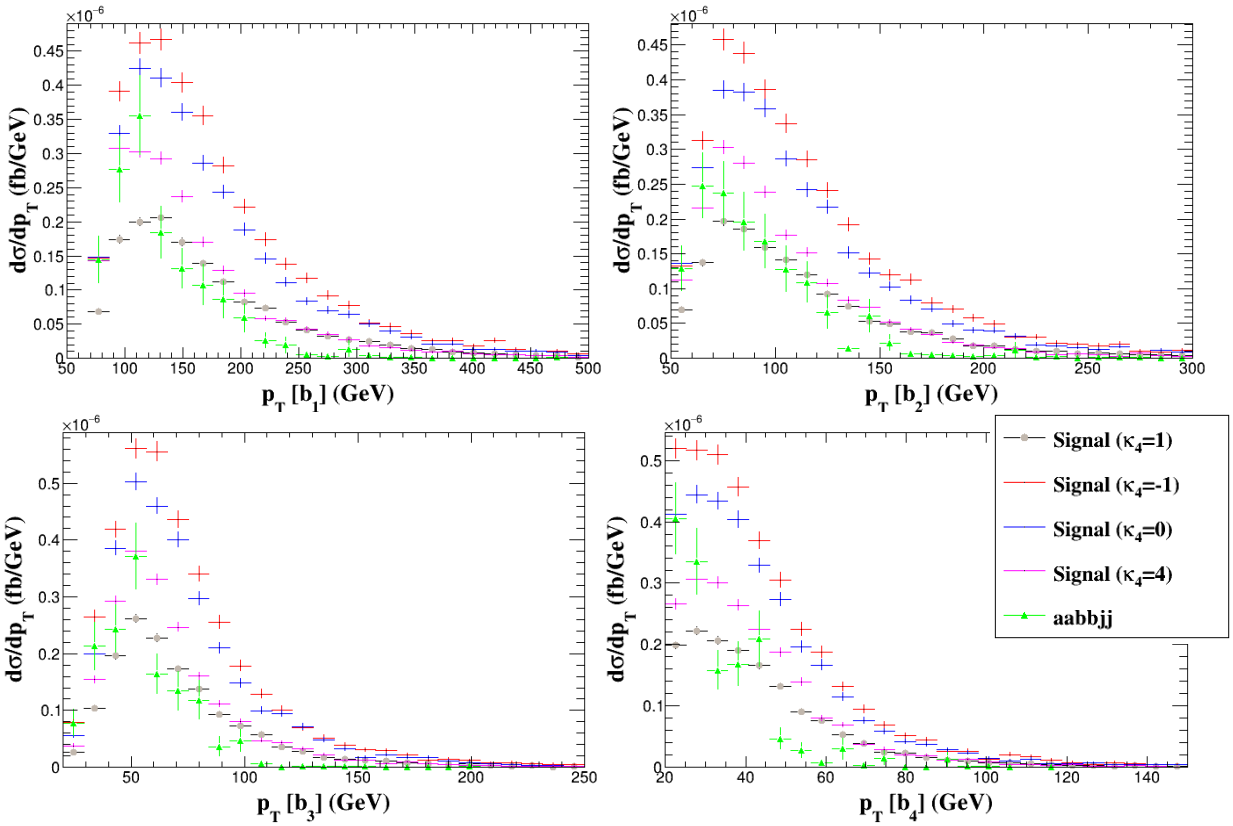

Figure 10: Transverse momentum distribution of the b-tagged jets for the triple-Higgs signal and the $\gamma\gamma b\bar{b}jj$ background. The signal is plotted of different values of the quartic scalar self-coupling, κ_4 (SM for $\kappa_4 = 1$).

D Plots with lower mistagging weight

We show here all studied log-scale distribution plots for the signal and the considered background. The mistagging rate has been set to more optimistic value: a mistagging rate of c and lighter jets as a b-jet of 1.8% and 0.1% respectively. The misidentification rate of jets as photons is 0.1%. This makes the background contamination much smaller, by a factor of 10^{-2}.

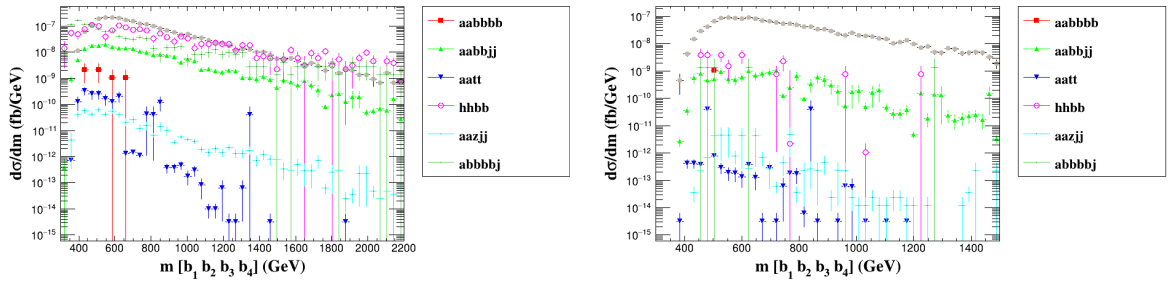

Figure 11: Invariant-mass distributions of the four leading b-tagged jets for the signal and background processes stated in Table 4. The plots on the left are before applying any event selection and the right ones are after event selection.

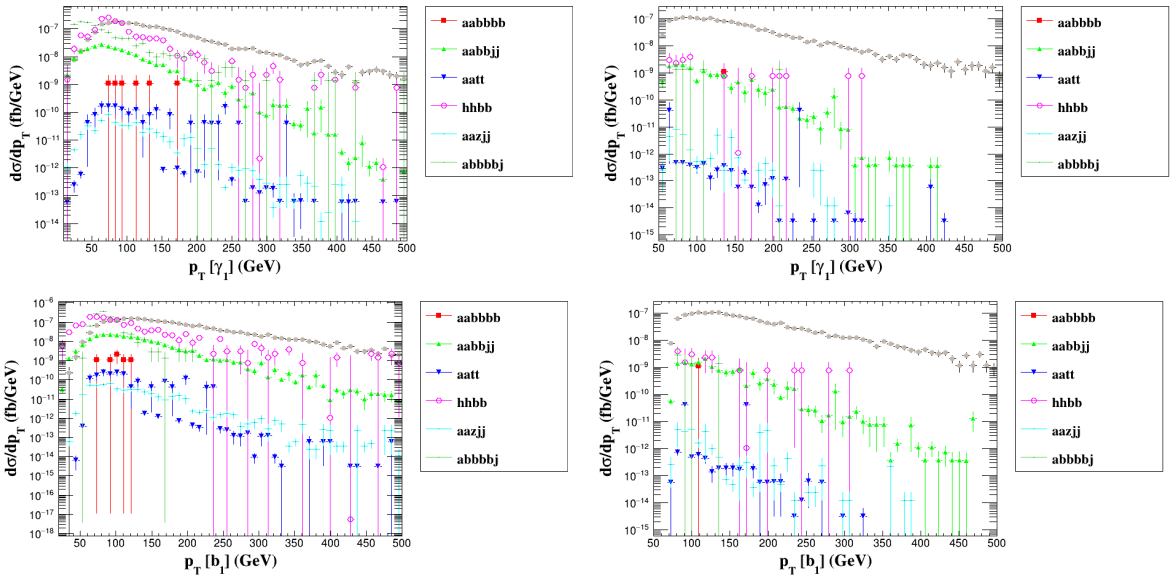

Figure 12: Transverse momentum distribution of the leading photon (the upper plots) and the leading b-tagged jets (the lower plots) for the signal and background processes stated in Table 4. The plots on the left are before applying any event selection and the right ones are after event selection.

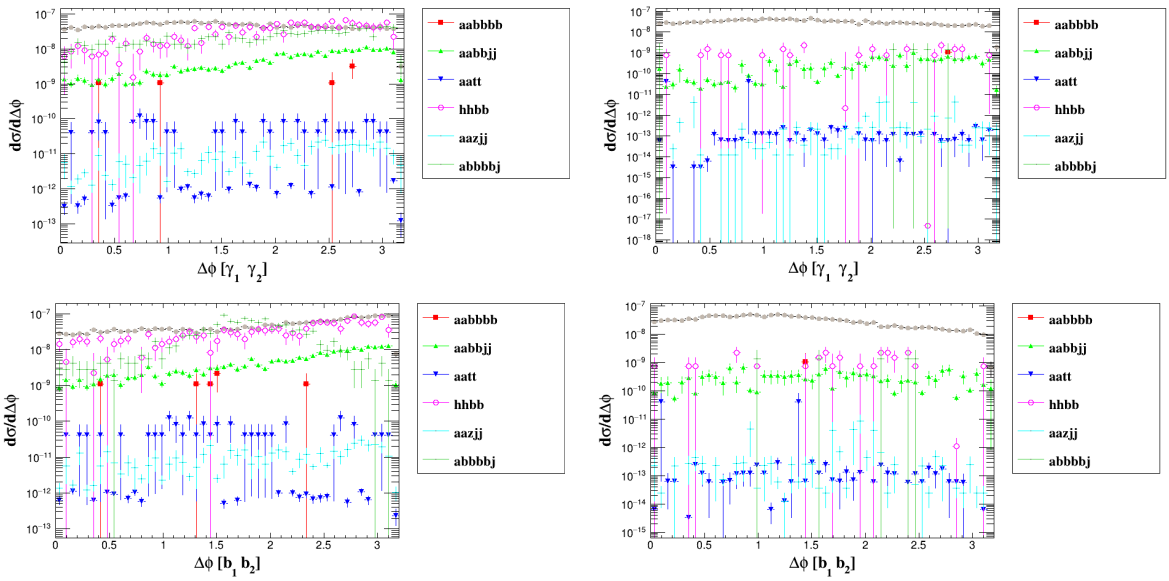

Figure 13: Azimuthal separation distribution between the leading photon (the upper plots) and the leading b-tagged jets (the lower plots) for the signal and background processes stated in Table 4. The plots on the left are before applying any event selection and the right ones are after event selection.

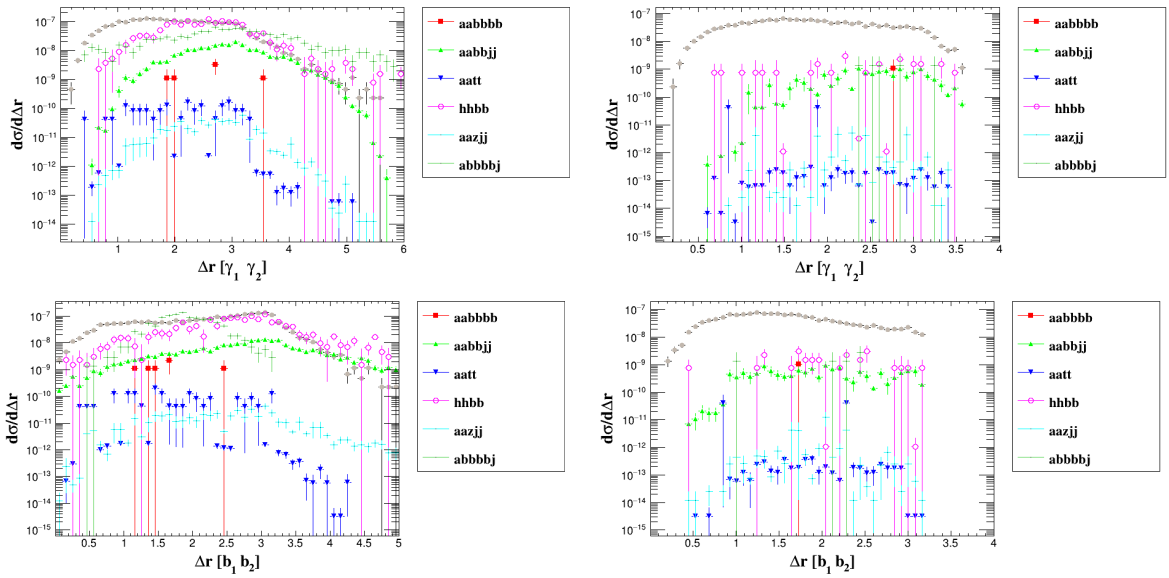

Figure 14: Angular distance (in the $\eta - \phi$ plane) distributions between the momentum of the leading photon (the upper plots) and b-tagged jets (the lower plots) for the signal and background processes stated in Table 4. The plots on the left are before applying any event selection and the right ones are after event selection.

E MadGraph run_card

The following is a summary of the MadGraph and Madspin synax used to generate the signal and background events.

Process	Syntax
Gluon fusion	generate g g > h h h QCD
Vector Bosons Fusion	generate p p > p p h h h
Top pair assc. prod.	generate g g > t t~ h h h
Vector Boson assc. prod.	define v = z w+ w-, generate p p > v h h h
Two top pair assc. prod.	generate p p > t t~ t t~ h h h QED=4
Single Top assc. prod.	generate p p > h h h t b~ j $$ w+ w- @0 add process p p > h h h t~ b j $$ w+ w- @1 add process p p > w- > h h h t~ b @1
$pp \to \gamma\gamma b\bar{b}jj$	generate p p > a a b b~ j j
$pp \to \gamma\gamma Zjj$	generate p p > a a z j j, z > b b~
$pp \to \gamma\gamma t\bar{t}$	generate p p > t t~ a a, (t > b w+, w+ > all all) (t~ > b~ w-, w- > all all)
$pp \to hhZ$	generate p p > h h z, z > b b~ , h > a a, h > b b~
$pp \to hZZ$	generate p p > h z z, z > b b~ , z > b b~ , h > a a
$pp \to hhjj$	generate > h h j j, h > a a, h > b b~
$pp \to hh\bar{b}\bar{b}$	generate g g > h h b b~ , h > a a, h > b b~
$pp \to h\bar{b}\bar{b}\bar{b}\bar{b}$	generate g g > h b b~ b b~ , h > a a
$pp \to \gamma\gamma bbbb$	generate p p > a a b b~ b b~
$pp \to \gamma\gamma ZZ$	generate p p > a a z z, z > b b~ , z > b b~
$pp \to \gamma b\bar{b}\bar{b}\bar{b}j$	generate p p > a b b~ b b~ j
$pp \to b\bar{b}\bar{b}\bar{b}jj$	generate p p > b b~ b b~ j j
Madspin Syntax	
No spin-correlation	set spinmode none
$h \to \gamma\gamma$	decay h > a a
$h \to b\bar{b}$	decay h > b b~
$h \to b\bar{b}$	decay h > b b~
$t \to W^+b, W^+ \to$ all all	decay t > w+ b, w+ > all all
$\bar{t} \to W^-\bar{b}, W^- \to$ all all	decay t~ > w- b~, w- > all all
$W^+ \to$ all all	decay w+ > all all
$W^- \to$ all all	decay w- > all all
$Z \to$ all all	decay z > all all

Table 7: The MadGraph and Madspin syntax used for generating the signal and background events. The model was a modified (as described in Section 2) version of "loop_sm" model provided by MG5aMC_2.6.7. The defined multiparticle shorthand notations are the default ones.